IEEE Access
Multidisciplinary ⋮ Rapid Review ⋮ Open Access Journal

Received February 14, 2022, accepted March 1, 2022, date of publication March 8, 2022, date of current version March 16, 2022.

Digital Object Identifier 10.1109/ACCESS.2022.3157629

3D Rotor Position-Dependant MEC Modeling of Different Claw Pole Machine Topologies

ROUA OMRI, AMINA IBALA, AND AHMED MASMOUDI, (Senior Member, IEEE)
Research Laboratory on Renewable Energies and Electric Vehicles (RELEV), ENIS, University of Sfax, Sfax 3038, Tunisia
Corresponding author: Roua Omri (roua.omri@enis.tn)

ABSTRACT The paper is aimed at a 3D magnetic equivalent circuit (MEC)-based modelling of claw pole synchronous machine topologies. Beyond the magnetic saturation and the armature magnetic reaction, the proposed modelling approach takes into consideration the rotor position variation, yielding the so-called: rotor position-dependant MEC. Accounting for the complexity of the magnetic circuit of claw pole topologies, specific assumptions are adopted prior a general analytical derivation of their MEC models. The developed analytical approach focuses on the air gap reluctance under variable rotor position considering a simplified geometry of the claw. A dedicated numerical procedure based on the Newton-Raphson algorithm is proposed for the resolution of the designed rotor position-dependant MEC. The proposed approach is applied to three claw pole topologies. The two first ones are equipped with a single source of excitation achieved by a field. Their analytically-predicted features are validated by experiments. The third topology has a dual excitation achieved by a field and permanent magnets (PMs) in the rotor. Its analytically-predicted features are validated by 3D finite element analysis (FEA). It is found that both experimental and FEA results are in quite good agreement with the analytical predictions yielded by the proposed rotor position-dependant MEC.

INDEX TERMS Armature magnetic reaction, claw pole topologies, magnetic saturation, no-/on-load features, rotor position-dependant magnetic equivalent circuit, single/dual excitation, three dimensional finite element analysis.

I. INTRODUCTION

The modelling of electric machines based on their magnetic equivalent circuits (MECs), also called lumped circuits, has been widely used [1], [2]. The great interest in MEC models is motivated by their simplicity and the low CPU time required for their resolution, compared to their finite element analysis (FEA) counterparts. These advantages are significantly highlighted when three dimensional (3D) models are required, as in the case of claw pole machines (CPM).

This said, MEC models have relatively lower accuracies compared to FEA ones. Moreover, it is quite commonly believed that MEC models suffer from their limited domain of validity. For instance, at a first glance, it appears that MEC models do not enable the investigation of time varying features. This statement is true in the case of static MECs which are derived for a single position of the rotor/mover. However, with the incorporation of the position of the moving part in the MEC, the investigation of the time varying feature turns to be feasible. The present work develops this idea with emphasis on the MEC modelling of different CPM topologies. Prior to do so, a literature review of the more recent works dealing with the MEC modelling of electric machines is presented hereunder.

In [3], Wang *et al.* proposed a hybrid excited synchronous machine. Beyond an excitation achieved by spoke type permanent magnets (PMs) in the rotor, the machine is equipped with two three phase ac winding: one is located in a cylindrical stator separated from the rotor by a radial airgap, and the other is linked to a plate-shaped stator mounted in the extremity of the radial one and separated from the rotor by an axial air gap. Two roles could be played separately by each three phase ac winding: (i) the torque production and (ii) the flux regulation. The latter has been analyzed thanks to simple MEC model considering four cases of hybrid excitation. Nevertheless, the MEC simplicity has been overextended considering just the reluctances of the two air gaps. Consequently, the MEC validity turned

The associate editor coordinating the review of this manuscript and approving it for publication was Jon Atli Benediktsson.

This work is licensed under a Creative Commons Attribution 4.0 License. For more information, see https://creativecommons.org/licenses/by/4.0/

to be limited to the case of linear magnetic circuit. In [4], Wang *et al.* investigated a transverse-flux brushless double-rotor machine mechanically-coupled to a traditional PM synchronous machine to play the role of a planetary gear of series-parallel hybrid propulsion systems. A 3D MEC of the transverse-flux machine has been developed which enabled the analysis of its main flux. Although the reluctances of the main leakage fluxes have been incorporated in the MEC, a significant shift has been found between the back-EMF predicted by the MEC and the experimental one. Such a weakness is due to the fact that the magnetic saturation has been neglected. In [5], Alipour-Sarabi *et al.* developed a MEC model of axial flux machines that takes into account the 3D flux paths and the rotor position variation. Moreover, the magnetic saturation, the flux fringing, the slot skewing, and the static and dynamic eccentricities have been incorporated in the proposed MEC. In spite of its complexity, it is shown that the results yielded by proposed model are in good agreement with the FEA ones along with a significant reduction of the CPU time in favor of the MEC. In [6], Zhang *et al.* proposed a torque motor with hybrid-magnetization pole arrays for jet pipe servo valve. The magnetic field distribution and the output torque of the proposed concept have been formulated considering a MEC model that takes into account the leakage flux of PMs and coils. The comparison between the analytical and FEA results has revealed some discrepancies caused by the assumption that neglects the magnetic saturation. This said, the authors underlined the fact that during the operation of aircrafts jet pipe electro-hydraulic servo valves, most rated currents of the torque motors are within 50 mA for which the magnetic circuit has a linear behavior. In [7], Saneie and Gheidari proposed a MEC model of an outer-rotor single phase squirrel cage induction motor. Beyond the rotor position, the developed MEC takes into account the rotor slots' skewing, the stator end windings, the slot leakage flux, and the magnetic saturation. Thanks to an appropriate coupling between the proposed MEC and the machine electrical equivalent circuit, the prediction of features such as the input and output powers turned to be feasible. A good agreement have been found between the analytical and experimental results. In [8], Yu *et al.* developed a MEC model of a PM slotted limited angle torque motor with nonuniform teeth. The proposed MEC takes into consideration the magnetic saturation, the armature magnetic reaction, and the rotor position variation. A MEC-based multi-objective optimization procedure has been developed in an attempt to improve the torque production capability. The accuracy of the obtained results highlighted the effectiveness of the developed MEC. In [9], Xu *et al.* investigated a transverse-flux linear oscillatory machine with PMs in the stator, intended for direct compressor drive. A nonlinear MEC has been derived in the case of on-load operation. In spite of its similar accuracy with respect to the 3D FEA one, the proposed MEC validity is limited to the analysis of the machine static features. In [10], Yang *et al.* proposed an outer rotor homopolar inductor machine for flywheel energy storage system. The analysis of the proposed concept has been carried out using a MEC model. However, the authors did not specify the considered assumptions nor the numerical procedure aimed at the resolution of the proposed MEC. Moreover, no comparison between MEC and FEA results was carried out.

Beyond conventional MECs that consider given number of loops through which flow the main and leakage fluxes, there is currently a trend that considers refined MEC models, the so-called "mesh based MECs". Despite their complexity, these models are reputed by their higher accuracy. In [11], Hemeida *et al.* proposed a mesh MEC model of surface axial flux PM synchronous machines. The proposed MEC is static but accounts for the rotor position via time-dependent PM magnetization sources. The investigation of the no- and full-load voltages, cogging torque, torque ripple, and stator iron core loss has been carried out using the developed mesh MEC model. In order to account for the nonlinear behavior of the magnetic circuit, the MEC has been iteratively-solved using the *Newton-Raphson* algorithm. In [12], Cao *et al.* proposed a mesh MEC model aimed at a multi-objective optimization of a surface-mounted PM. A parametric method has been considered in the mesh generation so that the MEC structure can be updated according to the changes of the reluctance network. Despite its high accuracy, the proposed has been established for a given slot-pole combination. By changing this latter would result in a change of the mesh node quantity and connections. Consequently, the proposed parametric structural transformation method would lose the merits of flexibility and efficiency.

CPMs have been the subject of intensive MEC-based analysis during the two last decades. These machines have been found viable candidates to generate electricity on board on most if not all road vehicles. This great interest is motivated by several advantages especially their heteropolar structure that enables the integration of high number of poles in a low volume. This said, CPMs suffer from some drawbacks, as: (i) the use of the brush-ring system which penalizes the machine compactness and reliability, (ii) the high leakage flux taking place between adjacent claws which compromises the torque production capability, and (iii) the high iron loss at high speeds especially those taking place in the rotor.

Design approaches have been proposed to reduce/eradicate the effects of the above limitations. The first one has been tackled by the transfer of the field from rotor to stator, yielding the so-called "stator-excited CPM" (SECPM) [13]. Such a transfer required appropriate changes of the magnetic circuit. The second limitation has been eliminated by inserting PMs between the claws, leading to the so-called "inter-pole PM hybrid excited CPM" (IPM-HECPM) [14]–[16]. Indeed, the PM flux is regarded as a second source of excitation as far as it is higher than the claw-to-claw linkage flux. An attempt to reduce the third limitation has been proposed in several works [17], [18]. It consists in substituting the solid iron rotor magnetic circuit by a soft magnetic composite made one.

Accounting for the 3D flux paths through the magnetic circuit of CPMs, an accurate prediction of their features requires complex 3D FEA procedures. Such a complexity characterizes the post processing step where the irregular air gap flux density along the axial direction has to be taken into consideration. CPM modelling and analysis could be suitably-achieved by 3D MECs whose validity could be improved by the incorporation of the rotor position. In [16], Tutelea *et al.* treated the modelling of a CPM integrating PMs between the claws in order to improve its output performance. The developed model is a 3D MEC that considers the rotation of the rotor equivalent circuit with respect to the stator one. The established MEC model has been used for the optimization of the machine using a non-linear iterative method based on the modified Hooke-Jeeves algorithm. The optimization procedure has led to an increase of the efficiency by 10% compared to one exhibited by the same CPM without PMs. In [14], Sim *et al.* proposed a PM assisted claw-pole synchronous motor. An infinitesimal hexahedron-element-based 3D MEC model has been developed in order to predict the motor features. The developed model takes into account the magnetic saturation and the rotor position variation. A comparison between the torque predicted by the proposed MEC and the one computed by 3D FEA revealed that the relative error remains lower than 2% with a reduction of a CPU time by 80%. In [19], Elloumi *et al.* developed a MEC model of a conventional CPM that takes into account the variation of the rotor position. For the sake of simplicity, the proposed MEC has been derived assuming that the rotor claws have a rectangular shape along the axial direction with an opening equal to the one of the machine median plane, leading to a 2D model. Furthermore, it has been established that, in order to achieve acceptable accuracies, both reluctance networks of the air gap and of the rotor claws have be updated when the rotor position varies. This has been carried out intuitively.

In this paper, the approach proposed in [19] has been totally rethought in order to take into account the 3D flux paths. Moreover, and for the sake of simplicity, only the air gap reluctance network is concerned by the rotor position variation. The air gap reluctance network is adapted using a rigourous analytical approach considering both direct and fringing flux tubes. The proposed 3D MEC modelling approach is applied to the prediction of the no- and on-load static and time-varying features of (i) a conventional CPM, (ii) a stator-excited CPM, and (iii) an IPM-HECPM.

II. ROTOR POSITION-DEPENDANT MEC: DESIGN APPROACH

In this section, the approach to predict the air-gap flux density distribution of CPMs using their 3D MEC models is inspired from the one developed in [20]. This latter has treated the case of synchronous reluctance machines with emphasis on the variation of air gap reluctance network with respect to the rotor position. For the sake of simplicity, some assumptions are adopted as given hereunder.

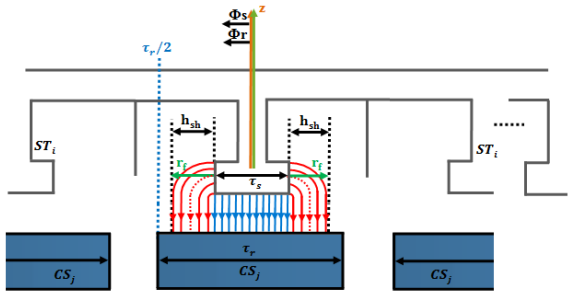

FIGURE 1. Air gap flux tubes. **Legend:** (blue) direct flux, (red) fringing flux.

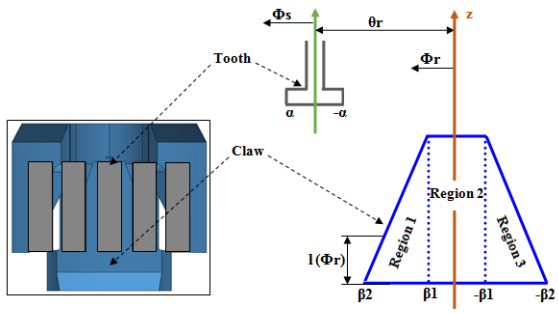

FIGURE 2. Surfaces shared by the stator teeth (in grey) and the rotor claws (in blue) within the air gap.

A. ADOPTED ASSUMPTIONS

It is assumed that only the air gap reluctance network is affected by the rotor position variation. Consequently, the air gap reluctance between the i-th stator tooth (STi) and the j-th section (CSj) of the claw surface facing the same stator tooth, is calculated considering the flux tubes shown in Fig. 1:

- the flux tube that involves the surface corresponding to the overlap between a stator tooth and a rotor claw within the air gap, yielding the so-called "direct flux tube",
- the flux tube circulating between a stator tooth shoe side and a rotor claw surface facing the air gap, leading to the so-called "fringing flux tube".

In case of no overlap between a stator tooth and a rotor claw, it is assumed that the involved reluctance is infinite.

B. ANALYSIS OF THE DIRECT FLUX TUBES

Fig. 2 shows the surfaces shared by the stator teeth (in grey) and the rotor claws (in blue) within the air gap. It also identifies three regions of the claw surface facing the air gap which will be considered in the formulation of the air gap reluctances. The one corresponding to the direct flux tube $\mathcal{R}_{ag}$ is derived using the *Hopkinson* law, as follows:

$$\mathcal{R}_{ag} = \frac{1}{\mu_0} \frac{g}{A_i} \tag{1}$$

where g and A_i are the air gap magnetic thickness, and surface facing region i with $(1 \leq i \leq 3)$ of the claw, respectively.

In Fig. 2, one can distinguish the following positions:

- ϕ_s corresponding to an angular position relative to a reference axis located in the middle of a stator tooth,
- ϕ_r corresponding to an angular position relative to a reference axis located in the middle of rotor claw, with:

$$\phi_r = \phi_s - \theta_r \tag{2}$$

where θ_r is the shift between the two axis.

In regions 1 and 3, the claw axial length depends on ϕ_r as:

$$l(\phi_r) = \frac{L_s}{\beta_2 - \beta_1}(\beta_2 - |\phi_r|) \tag{3}$$

where $(\beta_1 \leq |\phi_r| \leq \beta_2)$ and where L_s is the machine stack length which corresponds to the claw axial length in region 2.

Accounting for the positions of the tooth tip's edges ($-\alpha$ and α) as illustrated in Fig. 2, the air gap surface A_i facing region $i = 1, 3$ of the claw can be expressed as follows:

$$A_i = \frac{D}{2}\int_{\delta_1}^{\delta_2} l(\phi_r)d\phi_r \tag{4}$$

where D is the air gap diameter, and where the integral limits δ_1 and δ_2 depend on α, θ_r, β_1, and β_2.

Fig. 3 illustrates the possible cases of the air gap surface corresponding to the overlap between a stator tooth and regions i $(1 \leq i \leq 3)$ of a rotor claw.

1) CASE OF REGION 1

- Region1-case1

$$A_i = \frac{D}{2}\int_{-\alpha-\theta_r}^{\beta_2} l(\phi_r)d\phi_r \tag{5}$$

then:

$$\mathcal{R}_d = \frac{4g(\beta_2 - \beta_1)}{\mu_0 D L_s\left((\beta_2 + \alpha) + \theta_r\right)^2} \tag{6}$$

- Region1-case2

$$A_i = \frac{D}{2}\int_{-\alpha-\theta_r}^{\alpha-\theta_r} l(\phi_r)d\phi_r \tag{7}$$

then:

$$\mathcal{R}_d = \frac{g(\beta_2 - \beta_1)}{\mu_0 D L_s \alpha(\beta_2 + \theta_r)} \tag{8}$$

- Region1-case3

$$A_i = \frac{D}{2}\int_{\beta_1}^{\alpha-\theta_r} l(\phi_r)d\phi_r \tag{9}$$

then:

$$\mathcal{R}_d = \frac{4g(\beta_2 - \beta_1)}{\mu_0 D L_s\left((\beta_2 - \beta_1)^2 - ((\beta_2 - \alpha) + \theta_r)^2\right)} \tag{10}$$

2) CASE OF REGION 2

- Region2-case1

$$A_i = L_s\frac{D}{2}(\beta_1 + \alpha + \theta_r) \tag{11}$$

then:

$$\mathcal{R}_d = \frac{2g}{\mu_0 D L_s(\beta_1 + \alpha + \theta_r)} \tag{12}$$

- Region2-case2

$$A_i = L_s\frac{D}{2}2\alpha \tag{13}$$

then:

$$\mathcal{R}_d = \frac{g}{\mu_0 D L_s \alpha} \tag{14}$$

- Region2-case3:

$$A_i = L_s\frac{D}{2}(\beta_1 + \alpha - \theta_r) \tag{15}$$

then:

$$\mathcal{R}_d = \frac{2g}{\mu_0 D L_s(\beta_1 + \alpha - \theta_r)} \tag{16}$$

3) CASE OF REGION 3

- Region3-case1

$$A_i = \frac{D}{2}\int_{-\alpha-\theta_r}^{-\beta_1} l(\phi_r)d\phi_r \tag{17}$$

then:

$$\mathcal{R}_d = \frac{4g(\beta_2 - \beta_1)}{\mu_0 D L_s\left((\beta_2 - \beta_1)^2 - ((\beta_2 - \alpha) - \theta_r)\right)^2} \tag{18}$$

- Region3-case2

$$A_i = \frac{D}{2}\int_{-\alpha-\theta_r}^{\alpha-\theta_r} l(\phi_r)d\phi_r \tag{19}$$

then:

$$\mathcal{R}_d = \frac{g(\beta_2 - \beta_1)}{\mu_0 D L_s \alpha(\beta_2 - \theta_r)} \tag{20}$$

- Region3-case3

$$A_i = \frac{D}{2}\int_{-\beta_2}^{\alpha-\theta_r} l(\phi_r)d\phi_r \tag{21}$$

then:

$$\mathcal{R}_d = \frac{4g(\beta_2 - \beta_1)}{\mu_0 D L_s\left((\beta_2 + \alpha) - \theta_r\right)^2} \tag{22}$$

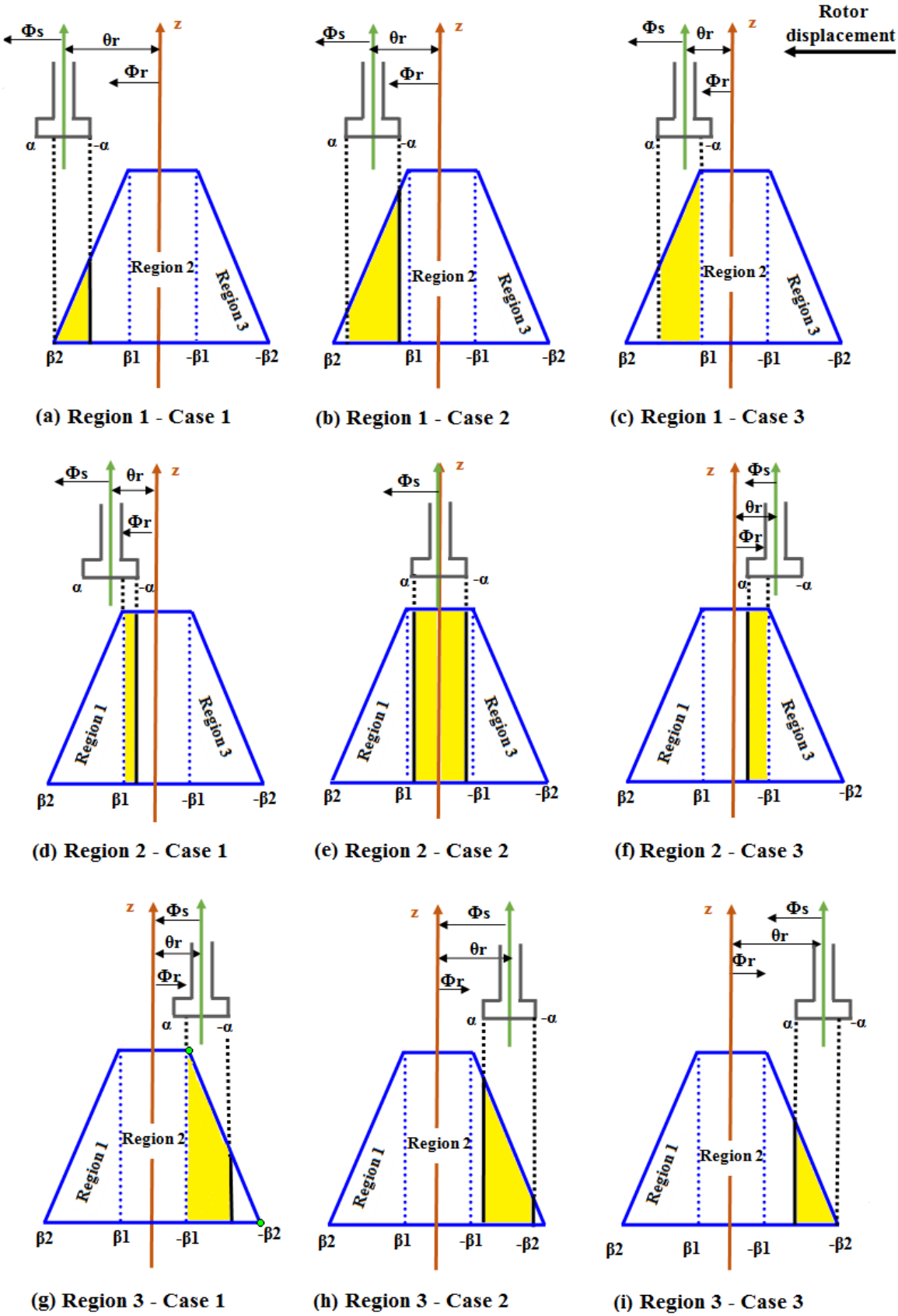

FIGURE 3. Possible cases of the air gap surface corresponding to the overlap between a stator tooth and regions i ($1 \leq i \leq 3$) of a rotor claw.

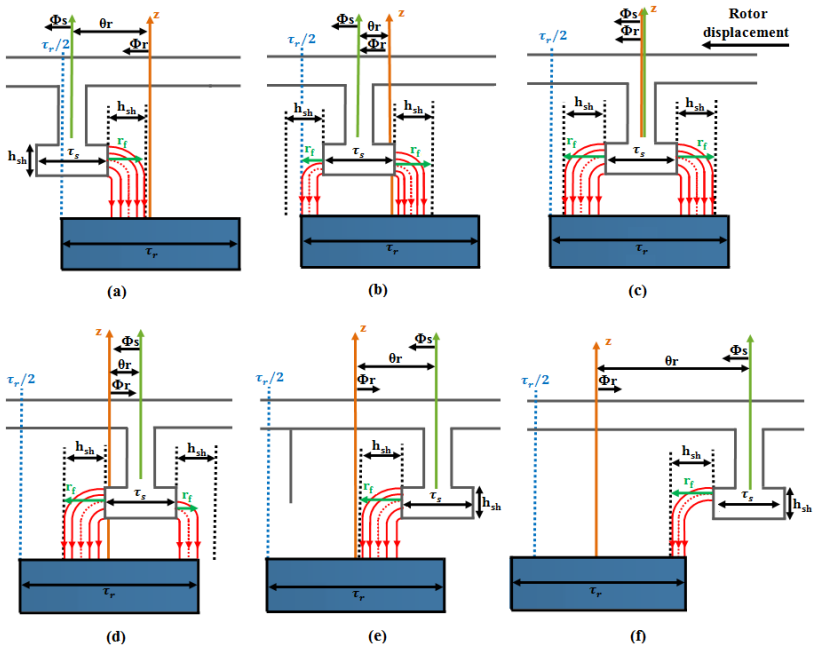

FIGURE 4. Possible cases of the fringing flux tube.

C. ANALYSIS OF THE FRINGING FLUX TUBES

The fringing flux has a nun-uniform path geometry where the flux tube length varies between equipotential surfaces, as depicted in Fig. 4. This makes the prediction of the permeance more convenient rather than the reluctance [21]. The equivalent length of a stator fringing flux tube is formulated as:

$$L_f = \frac{\pi}{2} r_f + g \tag{23}$$

where r_f is the radius characterizing the length of the fringing flux between the tooth side and the stator inner surface.

The fringing permeance $\mathcal{P}_f$ can be expressed as:

$$\mathcal{P}_f = \int_{r_{f1}}^{r_{f2}} \frac{\mu_0 L_s}{L_f} dr_f = \frac{2\mu_0 L_s}{\pi} \ln\left(\frac{\pi r_{f2} + 2g}{\pi r_{f1} + 2g}\right) \tag{24}$$

where r_{f1} and r_{f2} are the limits of integration defining the boundaries of the fringing flux tube.

Referring to Fig. 4, the fringing is characterized by two flux tubes, such that: (i) a right one with a permeance noted $\mathcal{P}_{fr}$, and (ii) a left one with a permeance noted $\mathcal{P}_{fl}$.

- Case 1: Referring to Fig. 4(a), one can notice that $\mathcal{P}_{fl}$ is null and that $\mathcal{P}_{fr}$ is characterized by $r_{f1} = 0$ and $r_{f2} = h_{sh}$, leading to:

$$\mathcal{P}_{fr} = \frac{2\mu_0 L_s}{\pi} \ln\left(\frac{\pi h_{sh}}{2g} + 1\right) \tag{25}$$

- Case 2: Referring to Fig. 4(b), $\mathcal{P}_{fr}$ has the same expression as in case 1 while $\mathcal{P}_{fl}$ is characterized by $r_{f1} = 0$ and $r_{f2} = R_{si}((\frac{\tau_r - \tau_s}{2}) + \theta_r)$ where R_{si} is the stator inner radius, τ_r and τ_s are the claw and stator shoe angular openings, respectively, leading to:

$$\mathcal{P}_{fl} = \frac{2\mu_0 L_s}{\pi} \ln\left(\frac{\pi R_{si}}{2g}\left(\left(\frac{\tau_r - \tau_s}{2}\right) + \theta_r\right)\right) \tag{26}$$

- Case 3 From Fig. 4(c), one can notice that θ_r=0, giving:

$$\mathcal{P}_{fr} = \mathcal{P}_{fl} = \frac{2\mu_0 L_s}{\pi} \ln\left(\frac{\pi h_{sh}}{2g} + 1\right) \tag{27}$$

- Case 4: Referring to Fig. 4(d), $\mathcal{P}_{fl}$ has the same expression as in case 3 while $\mathcal{P}_{fr}$ is characterized by $r_{f1} = 0$ and $r_{f2} = R_{si}((\frac{\tau_r - \tau_s}{2}) - \theta_r)$, leading to:

$$\mathcal{P}_{fr} = \frac{2\mu_0 L_s}{\pi} \ln\left(\frac{\pi R_{si}}{2g}\left(\left(\frac{\tau_r - \tau_s}{2}\right) - \theta_r\right)\right) \tag{28}$$

- Case 5: $\mathcal{P}_{fl}$ is the same as in case 4 and $\mathcal{P}_{fr}$ is null.

- Case 6: Referring to Fig. 4(f), one can notice that $\mathcal{P}_{fr}$ is null and that $\mathcal{P}_{fl}$ is characterized by $r_{f1} = R_{si}(\theta_r - (\frac{\tau_r + \tau_s}{2}))$ and $r_{f2} = h_{sh}$, leading to:

$$\mathcal{P}_{fl} = \frac{2\mu_0 L_s}{\pi} \ln\left(\frac{\pi h_{sh} + 2g}{\pi R_{si}(\theta_r - (\frac{\tau_r + \tau_s}{2})) + 2g}\right) \tag{29}$$

III. MEC RESOLUTION

In order to account for the nonlinear behavior of the magnetic circuit, a numerical procedure based on the *Newton-Raphson* algorithm incorporating the rotor position variation, has been developed. It has the flowchart shown in Fig. 5.

In the initial rotor position, the maximum possible relative permeability is considered in the expressions of the rotor reluctances. The derivation of the MEC is based on

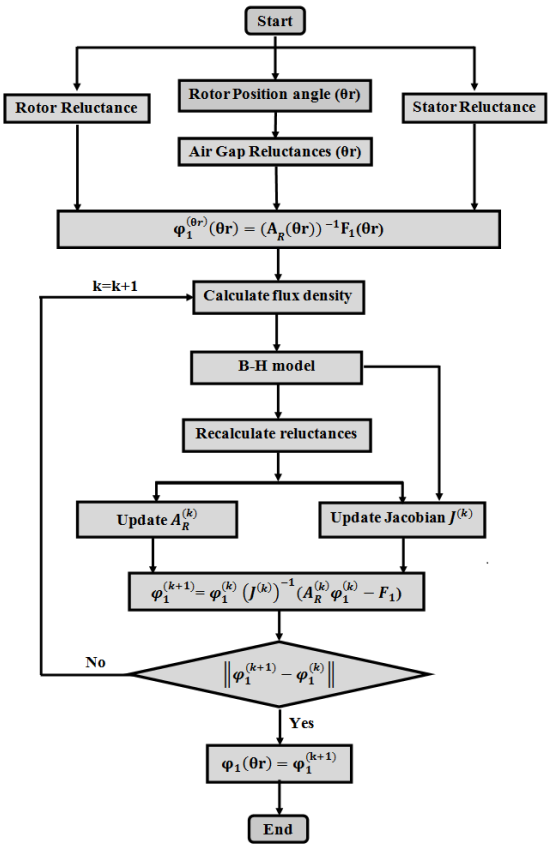

FIGURE 5. Flowchart of the developed numerical procedure dedicated to the resolution of the proposed MEC.

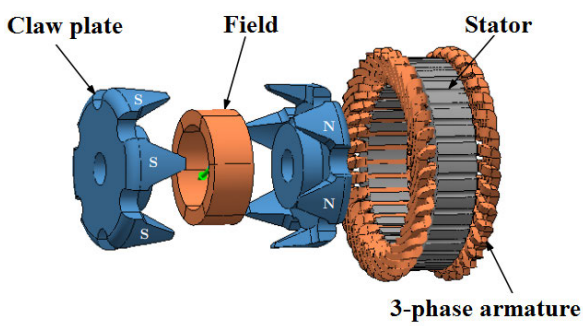

FIGURE 6. Exploded view of a CPM with a current excitation in the rotor.

the application of the Kirchhoff's law that has led to the following expression:

$$A_R^{(nl\times nl)}\varphi^{(nl\times 1)} = F^{(nl\times 1)} \tag{30}$$

where: A_R, φ and F represent the reluctance matrix, the vector of the loop fluxes, and the MMF vector, respectively.

The *B-H* characteristic of each material has enabled the prediction of $H(\frac{\varphi}{S})$ and then the involved reluctances. Once the *Jacobian* J and matrix A_R are updated, φ is predicted as follows [19]:

$$\varphi^{(k+1)} = \varphi^{(k)} - (J^{(k)})^{-1}(A_R^{(k)}\varphi^{(k)} - F) \tag{31}$$

TABLE 1. Influent stator geometric parameters.

Feature rated value	Symbol	Value
power at the rectifier output	P_r	1260W
DC current at the rectifier output	I_r	90A
DC voltage at the rectifier output	U_r	14V
speed	N_r	3000rpm

TABLE 2. Influent rotor geometric parameters.

Geometrical parameter	Symbol	Value (mm)
core length	l_{co}	26
core radius	R_{co}	23.42
claw plate thickness	th_p	10
claw plate height	h_p	12
claw base width	W_{bc}	23
claw tip height	h_{tc}	5
claw tip width	W_{tc}	7
rotor outer radius	R_r	48.9

TABLE 3. Influent stator geometric parameters.

Geometrical parameter	Symbol	Value (mm)
stator outer radius	R_{es}	63.8
stator inner radius	R_{is}	49.43
stator axial length	L_s	24.46
tooth height	h_{th}	10
tooth width	W_{th}	3.2
slot opening	s_{op}	2.4

IV. APPLICATION TO DIFFERENT CP TOPOLOGIES

A. CASE OF A CURRENT EXCITATION IN THE ROTOR

1) TOPOLOGICAL DESCRIPTION

Fig. 6 shows an exploded view of a CPM with a current excitation in the rotor. It is made up of:

- two overlapped solid iron claw plates in the rotor,
- a rotor axial core in between the two claw plates around which is wound the field,
- a stator lamination holding a three phase armature.

2) MEC DESIGN

Fig. 7 shows the developed MEC, for two rotor positions: $\theta_r = 0°$ and $\theta_r = 15°$, corresponding to the d- and q-axis, respectively. The 3D main flux paths are modeled by a MEC including:

- reluctances $\mathcal{R}_{syi}$, $\mathcal{R}_{thi}$, $\mathcal{R}_{csi}$, $\mathcal{R}_b$, $\mathcal{R}_p$, $\mathcal{R}_c$, and $\mathcal{R}_{ag}$ of the stator yoke, the stator teeth, the claw cross-section within the median axial plane, the claw bend, the claw plate, the rotor axial core, and the air gap, respectively,
- the MMF F_{dc} created by the field.

3) MEC-BASED PREDICTION OF THE MACHINE FEATURES

The CPM under study is equipped with 12 claws in the rotor, 36 slots in the stator, a three phase armature with a number of turns per coil equal to 20. It has the ratings listed in table 1, the influent geometrical parameters of rotor and stator given in tables 2 and 3, respectively, and an air gap width of 0.7mm.

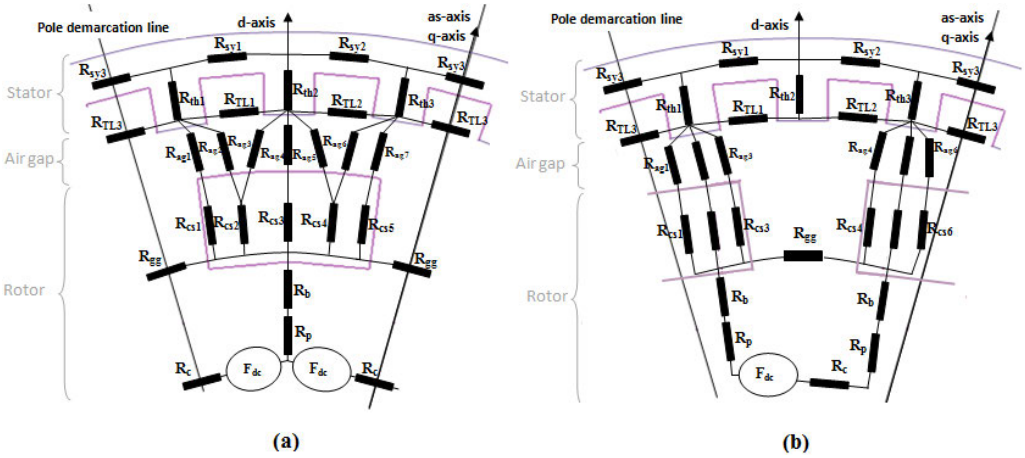

FIGURE 7. MEC of the CP machine with a current excitation in the rotor. Legend: (a) θ_r=0° (d-axis), (b) θ_r=15° (q-axis).

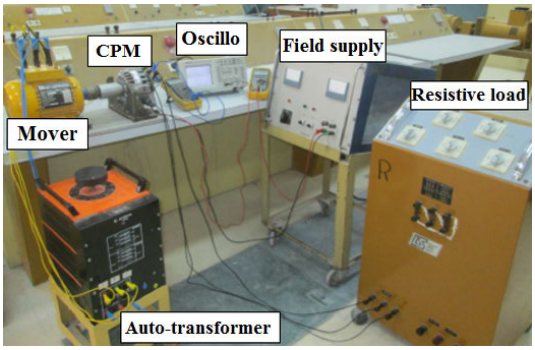

FIGURE 8. Developed test bench built around a CP machine equipped with a single current excitation in the rotor [19].

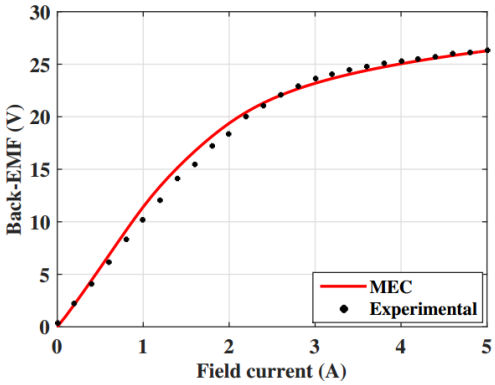

FIGURE 9. No-load characteristic for a speed of 2800rpm.Legend: (Red) MEC results, (black dots) experimental results.

The developed variable position MEC has been applied to the prediction of the machine features under no- and on-load operations. For the sake of validation of the MEC results, an experimental test bench has been built, as shown in Fig. 8.

a: NO-LOAD FEATURES

Fig. 9 depicts the no-load characteristic predicted by the developed MEC for a speed of 2800rpm. These results have been experimentally-validated.

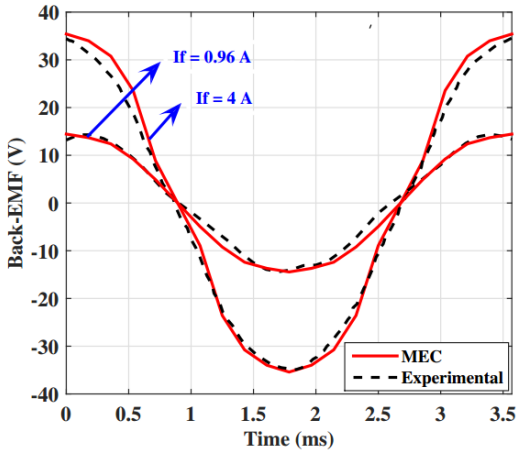

FIGURE 10. Back EMF waveforms for a speed of 2800rpm and two field currents of 0.96A and 4A. Legend: (Red) MEC results, (black dashes) experimental results.

Fig. 10 shows two back-EMF waveforms predicted for a speed of 2800rpm and for two field currents 0.96A and 4A. It also shows an experimental validation of the MEC results.

b: ON-LOAD FEATURES

Fig. 11 shows two on-load characteristics predicted considering a variable resistor in the armature for a speed of 2800rpm and two values of field current 0.96A and 4A. The figure also includes an experimental validation of the MEC results.

Fig. 12 shows the waveforms of the armature voltage predicted for a speed of 2800rpm, an armature current of 5.47A, and for two field currents 0.96A and 4A. Both Figs. 11 and 12 show an experimental validation of the MEC results.

4) MEC-BASED SIZING

In order to highlight the appropriateness of the proposed MEC for the machine design, it has been applied for the sizing of the air gap width with emphasis on the load characteristic, considering two values of the field current 0.96A and 4A. The obtained results are shown in the 3D plots of Fig. 13.

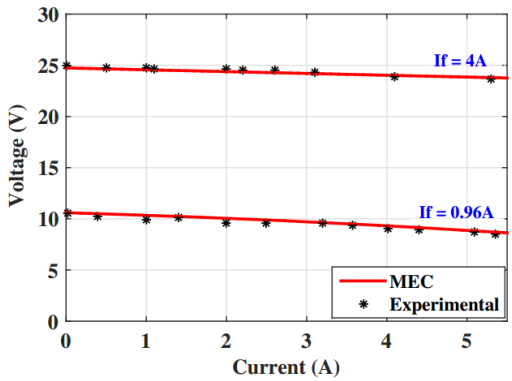

FIGURE 11. On-load characteristics under a variable resistor in the armature for a speed of 2800rpm and two field currents of 0.96A and 4A. Legend: (Red) MEC results, (black stars) experimental results.

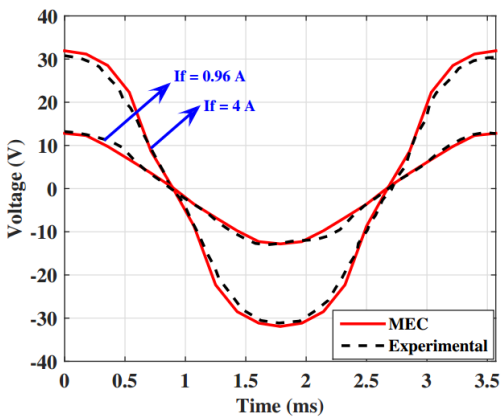

FIGURE 12. Armature voltage waveform for a speed of 2800rpm, an armature current of 5.47A, and two field currents of 0.96A and 4A. Legend: (Red) MEC results, (black dashes) experimental results.

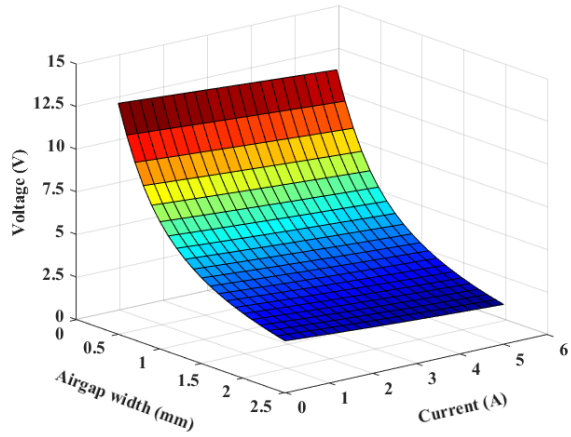

(a)

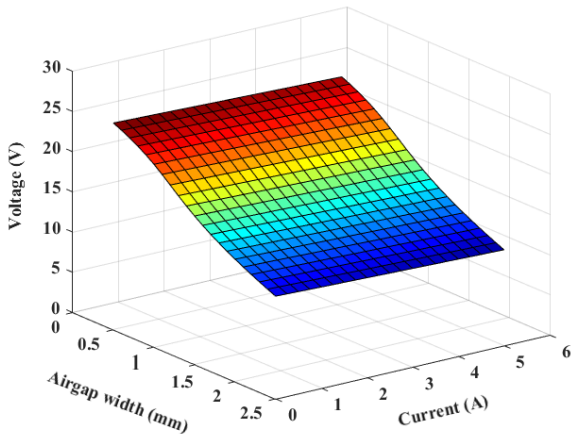

(b)

FIGURE 13. 3D plots giving the load characteristic of the a conventional CPM vs. the air gap width, under a variable resistor in the armature, for a speed of 2800rpm and for two values of the field current I_f. Legend (a) I_f=0.96A, (b) I_f=4A.

B. CASE OF A CURRENT EXCITATION IN THE STATOR

1) TOPOLOGICAL DESCRIPTION

Fig. 14 illustrates an exploded view of the claw pole machine equipped with a field in the stator. Compared to the topology studied in the previous paragraph, the main transformation consists in transferring the field from the rotor to the stator. Such a transformation required the topological changes enumerated herunder:

- ◇ the field is made up of the series connection of two concentrated coils inserted in both sides of the machine between the armature end-windings and the stator yoke,
- ◇ a yoke surrounding the stator lamination. It enables an axial circulation of the field flux,
- ◇ the plates holding the claws turn to be magnetically decoupled with the elimination of the rotor core surrounding the machine shaft,
- ◇ two magnetic collectors fixed on the machine flasks,
- ◇ two magnetic rings linked to the rotor and facing the magnetic collectors. The field flux circulates between the magnetic collectors and rings through an axial air gaps.

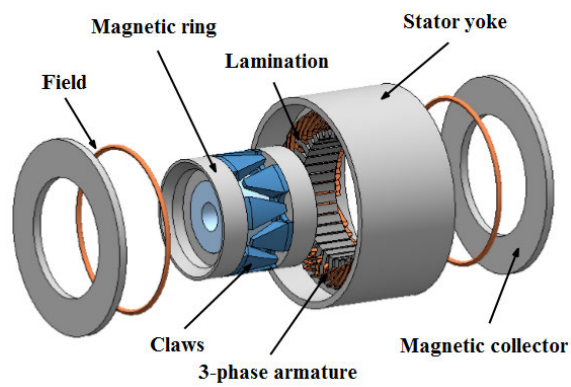

FIGURE 14. Exploded view of a CP machine with a current excitation in the stator.

2) MEC DESIGN

Fig. 15 shows the developed MEC where:

- $\mathcal{R}_{syi}$, $\mathcal{R}_{thi}$, $\mathcal{R}_{csi}$, and $\mathcal{R}_{ag}$: are similar to the ones of the rotor excited CP machine,

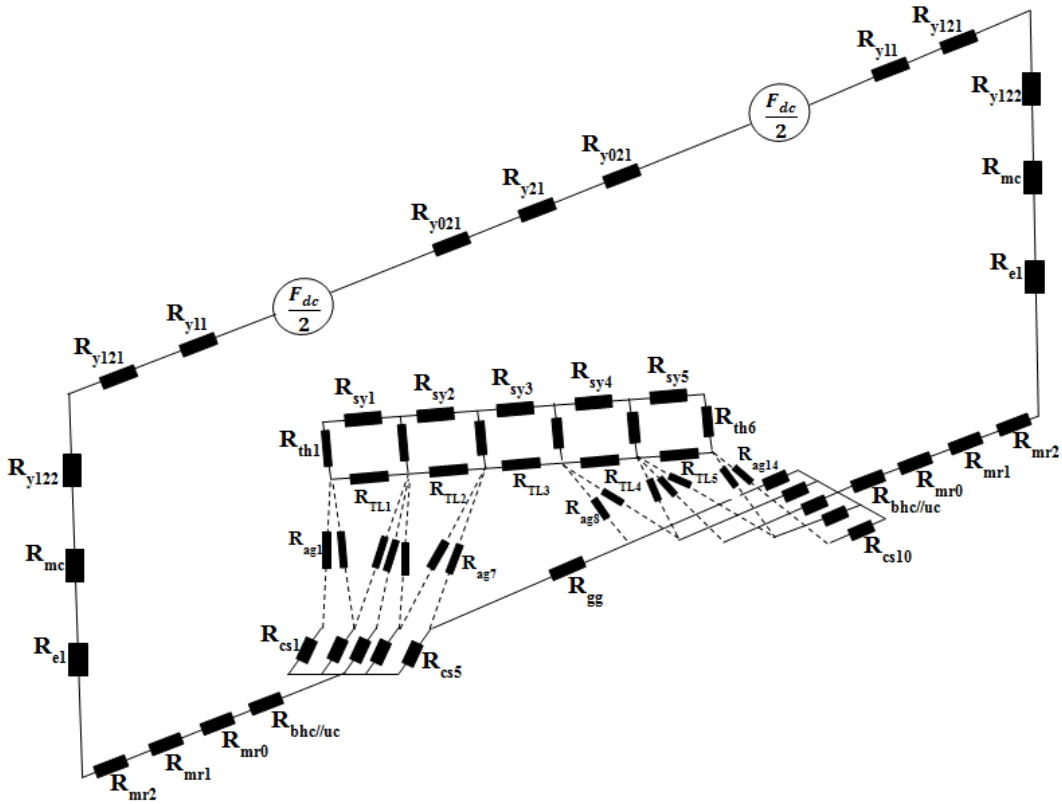

FIGURE 15. MEC of the CP machine with a current excitation in the stator.

- $\mathcal{R}_{y122}$, $\mathcal{R}_{y121}$, $\mathcal{R}_{y11}$, $\mathcal{R}_{y021}$, and $\mathcal{R}_{y21}$ are the yoke reluctances,
- $\mathcal{R}_{mc}$ is the magnetic collector reluctance,
- $\mathcal{R}_{e1}$ and R_{e2} are the axial air gap reluctances,
- $\mathcal{R}_{mr0}$, R_{mr1}, and R_{mr2} are the magnetic ring reluctances,
- $\mathcal{R}_{bhc}$ is the reluctance of the part behind claw,
- $\mathcal{R}_{uc}$ is the reluctance of the part under claw,
- F_{dc} is the MMF created by the field.

3) MEC-BASED PREDICTION OF THE MACHINE FEATURES

The developed variable position MEC has been applied to the prediction of machine features under no- and on-load operations. For the sake of validation of the MEC results, an experimental test bench has been built, as shown in Fig. 16. Photos of selected parts of the prototyped CPM equipped with a current excitation in the stator are depicted in Fig. 17.

The prototyped machine is equipped with 12 claws in the rotor, 36 slots in the stator, a three phase armature with a number of turns per coil equal to 56. Its ratings have been assessed and are listed in table 4. The influent geometrical parameters of rotor and stator are given in tables 5 and 6, respectively. It has a radial air gap with a width of 0.3mm and two axial air gaps located in both machine ends with a width of 0.26mm each.

a: NO-LOAD FEATURES

Using the proposed MEC, the prediction of the no-load characteristic has been achieved for a speed of 1000rpm.

TABLE 4. Influent stator geometric parameters.

Feature rated value	Symbol	Value
power	P_r	1440W
DC current at the rectifier output	I_r	30A
DC voltage at the rectifier output	U_r	48V
speed	N_r	1000rpm

TABLE 5. Influent rotor geometric parameters.

Geometrical parameter	Symbol	Value (mm)
core length	l_{co}	30.4
claw base width	W_{bc}	25
claw tip width	W_{tc}	5.8
under claw thickness	th_{uc}	4.34
behind claw thickness	th_{bhc}	7
rotor outer radius	R_r	44.84
magnetic ring length	l_{mr}	21

The obtained results are shown in Fig. 18. These results are experimentally-validated by the measurements illustrated by stars in the same figure.

Fig. 19 shows the waveform of the back-EMF predicted by the proposed MEC for a speed of 1000rpm and a field current of 5A. The same figure shows a single period of the back-EMF measured for the same speed and field current.

TABLE 6. Influent stator geometric parameters.

Geometrical parameter	Symbol	Value (mm)
stator outer radius	R_{es}	62
stator inner radius	R_{is}	45.16
stator axial length	L_s	29.1
yoke length	L_y	82.26
yoke height	h_y	5.3
tooth height	h_{th}	11
tooth width	W_{th}	3
slot opening	s_{op}	2.9
magnetic collector height	h_{mc}	17.1
magnetic collector width	W_{mc}	6.02

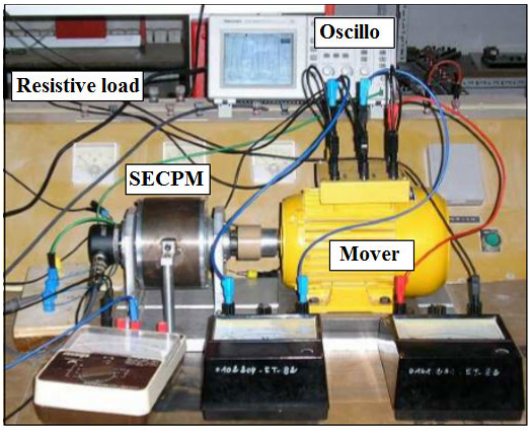

FIGURE 16. Developed test bench built around a CPM equipped with a current excitation in the stator [13].

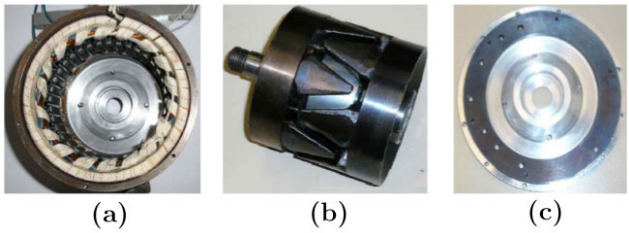

FIGURE 17. Prototyped machine. Legend: (a) stator, (b) rotor, (c) a flask showing the magnetic collector (in black).

b: ON-LOAD FEATURES

The investigation of the stator-excited CPM has been extended to the on-load operation, considering the case of a variable resistor connected to the armature for a speed of 1000rpm. The developed MEC is first applied for the prediction of the load-characteristic for a field current of 5A. The obtained results are shown in Fig. 20. The MEC-based prediction of the armature voltage for a speed of 1000rpm, an armature current of 0.6A, and a field current of 5A, has led to the waveform depicted in Fig. 21.

The on-load features predicted by the developed MEC are experimentally-validated in Figs. 20 and 21.

4) MEC-BASED SIZING

The proposed MEC is a powerful tool for the sizing of the stator-excited CPM. For instance, it has been applied in this work for the sizing of the widths of both radial and axial air gaps with emphasis on the load characteristic, considering a variable resistive load in the armature, for a speed of 1000rpm and a field current of 5A. The obtained results are shown in the 3D plots of Fig. 22.

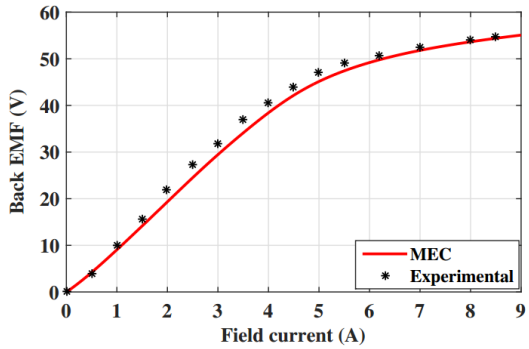

FIGURE 18. No-load characteristic for a speed of 1000rpm. Legend: (Red) MEC results, (black stars) experimental results.

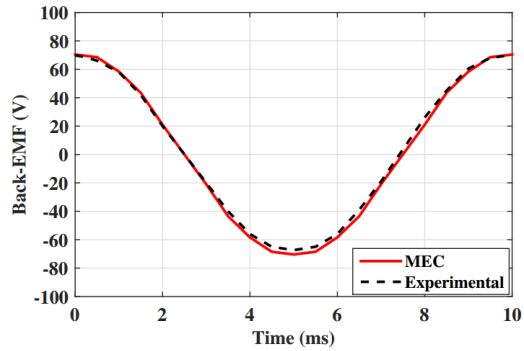

FIGURE 19. Back-EMF waveform for a speed of 1000rpm and a field current of 5A. Legend: (Red) MEC results, (black dashes) experimental results.

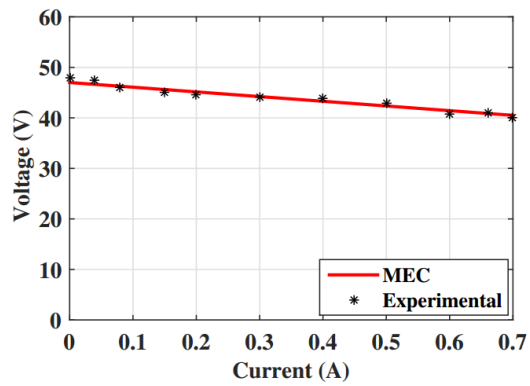

FIGURE 20. On-load characteristic under a variable resistor in the armature for a speed of 1000rpm and a field current of 5A. Legend: (Red) MEC results, (black stars) experimental results.

C. CASE OF A DUAL EXCITATION IN THE ROTOR

1) TOPOLOGICAL DESCRIPTION

Fig. 23 illustrates an exploded view of the IPM-HECPM under study. It has almost the same topology as the CP

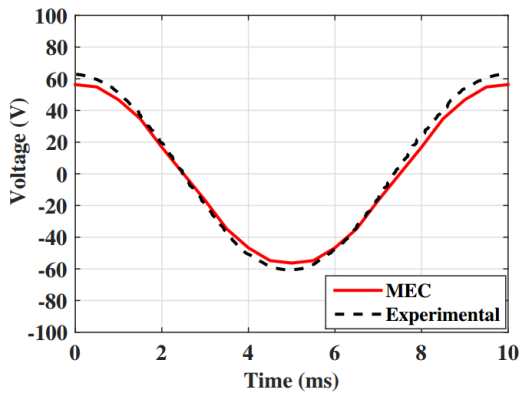

FIGURE 21. Armature voltage waveform for a speed of 1000rpm, an armature current of 0.6A, and a field current of 5A. **Legend:** (Red) MEC results, (black dashes) experimental results.

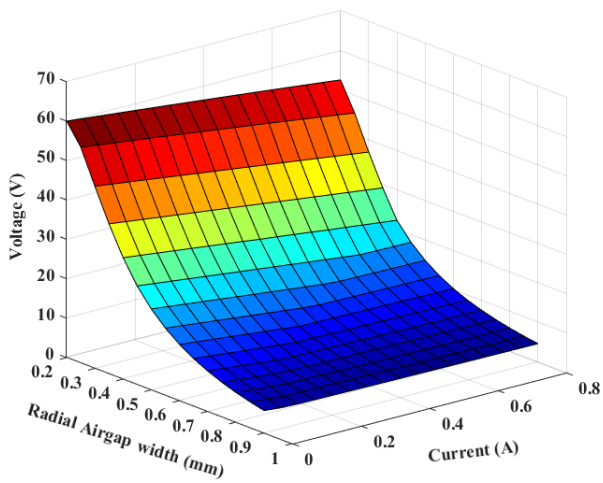

(a)

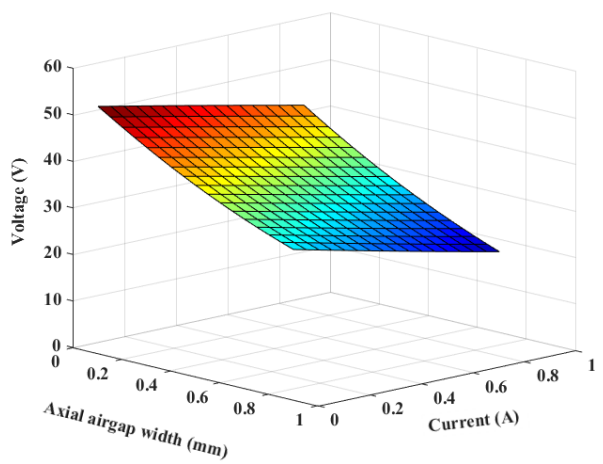

(b)

FIGURE 22. 3D plots giving the load characteristic of the stator-excited CPM vs. the air gap width, under a variable resistor in the armature, for a speed of 1000rpm and for a field current of 5A. **Legend** (a) sizing of the radial air gap, (b) sizing of the axial air gap.

machine treated in paragraph IV-A. Both topologies differ by the PMs inserted in between the claws as shown in Fig. 23.

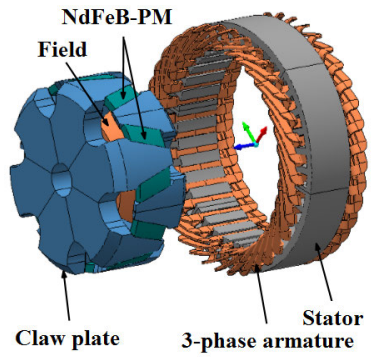

FIGURE 23. Exploded view of the IPM-HECPM.

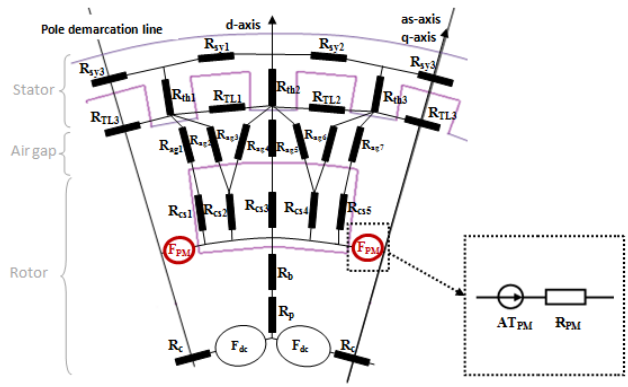

FIGURE 24. MEC of the of the IPM-HECPM.

Basically, these have been incorporated in order to face the claw-to-claw leakage flux. However, the flux generated by the NdFeB PMs is by far higher than the targeted leakage flux. The PM extra flux represents a second source of excitation. Hence, the machine turns to be equipped with two sources of excitation: (i) a main source achieved by the field wound around the rotor core, and (ii) an auxiliary source achieved by the PMs inserted in between the claws.

2) MEC DESIGN

The developed MEC of the IPM-HECPM under study is illustrated in 24. It is similar to the one shown in Fig. 7(a); the only difference is the PM MEC shown in the dashed box of Fig. 24. The PM is characterized by a remanence B_r, a magnetic permeability μ_{PM}, a section S_{PM} and a length L_{PM}. The PM MMF and reluctance, noted AT_{PM} and $\mathcal{R}_{PM}$, respectively, are expressed as follows:

$$\begin{cases} AT_{PM} = \dfrac{L_{PM} B_r}{\mu_{PM}} \\ \mathcal{R}_{PM} = \dfrac{L_{PM}}{\mu_{PM} S_{PM}} \end{cases} \tag{32}$$

3) MEC-BASED PREDICTION OF THE MACHINE FEATURES

The MEC shown in Fig. 24 has been applied to the prediction of the no- and on-load features covering both static and

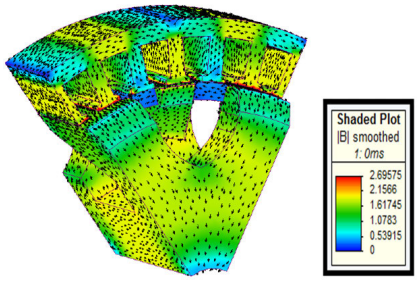

FIGURE 25. Flux density mapping across the IPM-HECPM magnetic circuit under no-load operation for a field current of 4A.

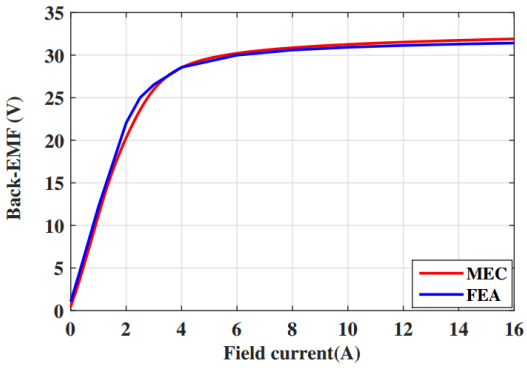

FIGURE 26. No-load characteristic for a speed of 2800rpm. Legend: (Red) MEC, (blue) 3D-FEA.

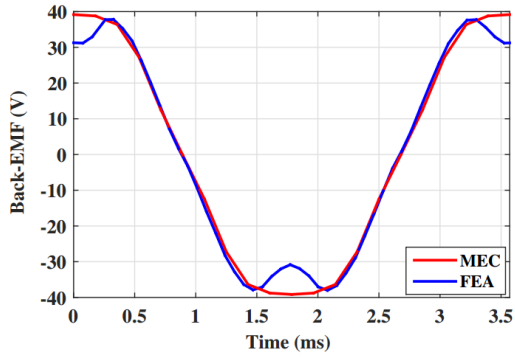

FIGURE 27. Back-EMF waveform for a speed of 2800 rpm and a field current of 4A. Legend: (Red) MEC, (blue) 3D-FEA.

time-varying ones. These are validated by a 3D FEA model, developed using a MagNet software package.

The IPM-HECPM under study has the influent geometrical parameters of rotor and stator given in tables 2 and 3, respectively, and an air gap width of 0.7mm. Furthermore, it is equipped with NdFeB PM blocs in between the claws with a remanence of 1.028T and a cœrcitivity of 818kA/m.

a: NO-LOAD FEATURES

Fig. 25 gives the flux density mapping computed by FEA for a field current I_f of 4A. In spite of the low value of I_f, one can notice, from the scale of Fig. 25, that the flux

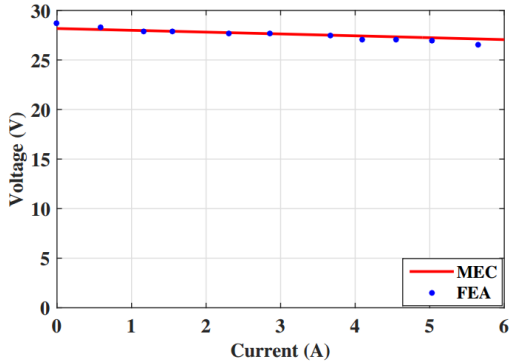

FIGURE 28. On-load characteristic for a speed of 2800rpm and a field current of 4A. Legend: (Red) MEC, (blue) 3D-FEA.

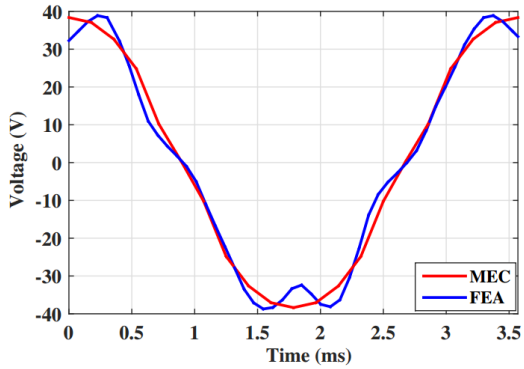

FIGURE 29. Armature voltage for a speed of 2800rpm, an armature current of 5.47A, and a field current of 4A. Legend:(Red) MEC, (blue) 3D-FEA.

density reaches almost 2.7T. Focusing such a high level of saturation, it has been found that it is located in minor sharp geometrical imperfections in the drawing of the study domain.

Fig. 26 shows the MEC-predicted no-load characteristic along with its FEA validation. As expected, for a given field current, the IPM-HECPM generates a higher back-EMF than the one of the CPM treated in paragraph IV-A. Moreover, using a HP Z440 Workstation with a processor of Intel(R) CPU E5-1620 v3 @3.50GHz and a RAM of 16,0 Go, the MEC-predicted no-load characteristic took just 4min50s while the one computed by FEA required a CPU-time of 47H22min.

Fig. 27 shows the waveform of the back-EMF predicted by the proposed MEC for a speed of 2800rpm and a field current of 4A, along with its FEA validation. One can remark the existence of disparities within the maximum values between the MEC and FEA results. These are due to the high levels of saturation already revealed by the flux density mapping of Fig. 25. In spite of the similarity of the B-H curves implemented in the MEC model and in the FEA one, the latter exhibits high levels of saturation due to minor sharp geometrical imperfections in the study domain drawing.

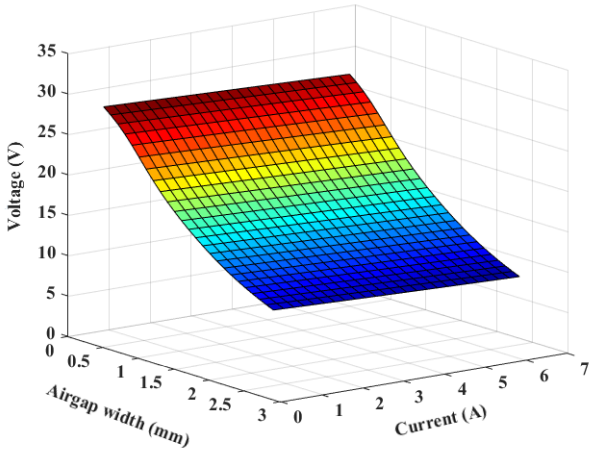

(a)

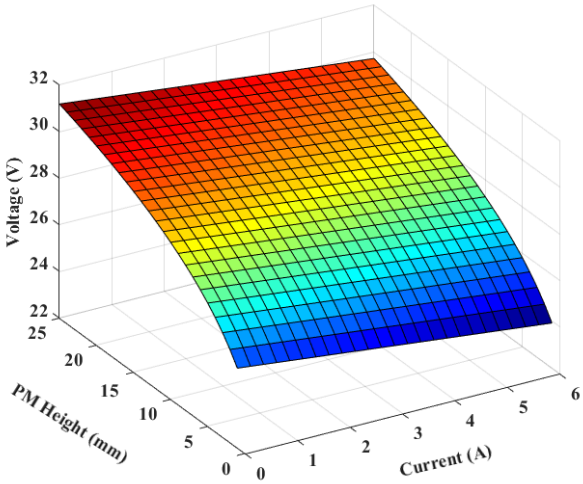

(b)

FIGURE 30. 3D plots giving the load characteristic of the IPM-HECPM vs. the air gap width and the PM hight, under a variable resistor in the armature, for a speed of 1000rpm and for a field current of 4A. Legend (a) sizing of the air gap, (b) sizing of the PM height.

b: ON-LOAD FEATURES

Figs. 28 and 29 show the on-load characteristic and the armature voltage waveform predicted by the proposed MEC and validated by FEA, considering a variable resistor in the armature, for a speed of 2800rpm and a field current of 4A. The interpretation of the disparities noticed in Fig. 27 remains applicable for Fig. 29.

4) MEC-BASED SIZING

The proposed MEC has been applied for the sizing of the IPM-HECPM, by selecting the air gap width and the PM height with emphasis on the load characteristic, considering a variable resistive load in the armature, for a speed of 2800rpm and a field current of 4A. The obtained results are shown in the 3D plots of Fig. 30.

V. CONCLUSION

The paper was aimed at the MEC modeling of three claw pole machine (CPM) topologies, namely: (i) a conventional CPM, (ii) a stator-excited CPM, and an inter-pole PM hybrid excited CPM. The validity of the proposed models has been extended to the investigation of the time-varying features thanks to the incorporation of the rotor position variation. Accounting for the complexity of the magnetic circuit of claw pole topologies, specific assumptions were adopted prior the derivation of the MEC models with emphasis on the changes of the air gap reluctances under variable rotor position considering a simplified geometry of the claws. A dedicated numerical procedure based on the Newton-Raphson algorithm has been developed for the MEC resolution. The results yielded by the proposed MECs have been validated by experiments in the case of the conventional and stator-excited CPMs and by 3D-FEA in the case of inter-pole PM hybrid excited one.

REFERENCES

[1] I. Eguren, G. Almandoz, A. Egea, X. Badiola, and A. Urdangarin, "Understanding switched-flux machines: A MMF-permeance model and magnetic equivalent circuit approach," *IEEE Access*, vol. 10, pp. 6909–6928, 2022.

[2] G. Watthewaduge and B. Bilgin, "Radial force density calculation of switched reluctance machines using reluctance mesh-based magnetic equivalent circuit," *IEEE Open J. Ind. Electron. Soc.*, vol. 3, pp. 22–49, 2022.

[3] D. Wang, D. Zhang, D. Xue, C. Peng, and X. Wang, "A new hybrid excitation permanent magnet machine with an independent AC excitation port," *IEEE Trans. Ind. Electron.*, vol. 66, no. 8, pp. 5872–5882, Aug. 2019.

[4] M. Wang, P. Zheng, C. Tong, Q. Zhao, and G. Qiao, "Research on a transverse-flux brushless double-rotor machine for hybrid electric vehicles," *IEEE Trans. Ind. Electron.*, vol. 66, no. 2, pp. 1032–1043, Feb. 2019.

[5] R. Alipour-Sarabi, Z. Nasiri-Gheidari, and H. Oraee, "Development of a three-dimensional magnetic equivalent circuit model for axial flux machines," *IEEE Trans. Ind. Electron.*, vol. 67, no. 7, pp. 5758–5767, Jul. 2020.

[6] Q. Zhang, L. Yan, Z. Duan, Z. Jiao, C. Gerada, and I.-M. Chen, "High torque density torque motor with hybrid magnetization pole arrays for jet pipe servo valve," *IEEE Trans. Ind. Electron.*, vol. 67, no. 3, pp. 2133–2142, Mar. 2020.

[7] H. Saneie and Z. Nasiri-Gheidari, "Performance analysis of outer-rotor single-phase induction motor based on magnetic equivalent circuit," *IEEE Trans. Ind. Electron.*, vol. 68, no. 2, pp. 1046–1054, Feb. 2021.

[8] G. Yu, Y. Xu, T. Lin, L. Xiao, J. Zou, and J. Tan, "Nonlinear EMC modeling and analysis of permanent-magnet slotted limited-angle torque motor," *IEEE Trans. Ind. Electron.*, vol. 68, no. 9, pp. 8507–8518, Sep. 2021.

[9] W. Xu, X. Li, J. Zhu, and Q. Wang, "3-D modeling and testing of a stator-magnet transverse-flux linear oscillatory machine for direct compressor drive," *IEEE Trans. Ind. Electron.*, vol. 68, no. 9, pp. 8474–8486, Sep. 2021.

[10] J. Yang, C. Ye, and S. Huang, "Development and analysis of an outer rotor homopolar inductor machine for flywheel energy storage system," *IEEE Trans. Ind. Electron.*, vol. 68, no. 8, pp. 6504–6515, Aug. 2021.

[11] A. Hemeida, A. Lehikoinen, P. Rasilo, H. Vansompel, A. Belahcen, A. Arkkio, and P. Sergeant, "A simple and efficient quasi-3D magnetic equivalent circuit for surface axial flux permanent magnet synchronous machines," *IEEE Trans. Ind. Electron.*, vol. 66, no. 11, pp. 8318–8333, Nov. 2019.

[12] D. Cao, W. Zhao, J. Ji, and Y. Wang, "Parametric equivalent magnetic network modeling approach for multiobjective optimization of PM machine," *IEEE Trans. Ind. Electron.*, vol. 68, no. 8, pp. 6619–6629, Aug. 2021.

[13] A. Ibala and A. Masmoudi, "Accounting for the armature magnetic reaction and saturation effects in the reluctance model of a new concept of claw-pole alternator," *IEEE Trans. Magn.*, vol. 46, no. 11, pp. 3955–3961, Nov. 2010.

[14] J.-H. Sim, D.-G. Ahn, D.-Y. Kim, and J.-P. Hong, "Three-dimensional equivalent magnetic circuit network method for precise and fast analysis of PM-assisted claw-pole synchronous motor," *IEEE Trans. Ind. Appl.*, vol. 54, no. 1, pp. 160–171, Jan./Feb. 2018.

[15] Y. Li, Z. Yu, H. Meng, J. Wang, and Y. Jing, "Design and optimization of hybrid-excited claw-pole machine for vehicle," *IEEE Trans. Appl. Supercond.*, vol. 31, no. 8, pp. 1–4, Nov. 2021, doi: 10.1109/TASC.2021.3094433.

[16] L. Tutelea, D. Ursu, I. Boldea, and S. Agarlita, "IPM claw-pole alternator system for more vehicle braking energy recuperation," *J. Elec. Eng.*, vol. 12, no. 3, pp. 1–10, 2012.

[17] C. Liu, G. Lei, T. Wang, Y. Guo, Y. Wang, and J. Zhu, "Comparative study of small electrical machines with soft magnetic composite cores," *IEEE Trans. Ind. Electron.*, vol. 64, no. 2, pp. 1049–1060, Feb. 2017.

[18] W. Du, S. Zhao, H. Zhang, M. Zhang, and J. Gao, "A novel claw pole motor with soft magnetic composites," *IEEE Trans. Magn.*, vol. 57, no. 2, pp. 1–4, Feb. 2021, doi: 10.1109/TMAG.2020.3019830.

[19] D. Elloumi, A. Ibala, R. Rebhi, and A. Masmoudi, "Lumped circuit accounting for the rotor motion dedicated to the investigation of the time-varying features of claw pole topologies," *IEEE Trans. Magn.*, vol. 51, no. 5, pp. 1–8, May 2015, doi: 10.1109/TMAG.2015.2405896.

[20] M. L. Bash, J. M. Williams, and S. D. Pekarek, "Incorporating motion in mesh-based magnetic equivalent circuits," *IEEE Trans. Energy Conver.*, vol. 25, no. 2, pp. 329–338, Jun. 2010.

[21] M. Cheng, K. T. Chau, C. C. Chan, E. Zhou, and X. Huang, "Nonlinear varying-network magnetic circuit analysis for doubly salient permanent-magnet motors," *IEEE Trans. Magn.*, vol. 36, no. 1, pp. 339–348, Jan. 2000.

ROUA OMRI received the B.S. degree in electrical engineering and the M.S. degree in sustainable mobility actuators: research and technology (SMART) from the Sfax Engineering National School (SENS), University of Sfax, Tunisia, in 2016 and 2017, respectively, where she is currently pursuing the Ph.D. degree with the Research Laboratory of Renewable Energies and Electric Vehicles (RELEV). Her Ph.D. works dealt with the 3D MEC and FEA modeling of different topologies of claw pole machines.

AMINA IBALA received the B.S. degree in electromechanical engineering, the M.S. degree in electric machine analysis and control, and the Ph.D. degree in electrical engineering from the Sfax Engineering National School (SENS), University of Sfax, Tunisia, in 2006, 2007, and 2011, respectively, where she is currently pursuing the Postdoctoral Habilitation degree with the Research Laboratory of Renewable Energies and Electric Vehicles. She is currently a member of the Research Laboratory of Renewable Energies and Electric Vehicles. Her major interests include the design, modeling, and optimization of claw pole machine topologies equipped with single- and hybrid-excitation.

AHMED MASMOUDI (Senior Member, IEEE) received the B.S. degree (long term) in electrical engineering from the Sfax Engineering National School (SENS), University of Sfax, Sfax, Tunisia, in 1984, the Ph.D. degree in electrical engineering from Pierre and Marie Curie University, Paris, France, in 1994, and the Postdoctoral Research Habilitation degree in electrical engineering from SENS, in 2001.

In 1988, he joined Tunisian University, where he held different positions involved in both education and research activities. He is currently a Full Professor of electric power engineering with SENS. He is the Head of the Research Laboratory on Renewable Energies and Electric Vehicles and the Coordinator of the Master on Sustainable Mobility Actuators: Research and Technology. He is the author of more than 100 papers, 27 among which are published in IEEE Transactions. He is the author and coauthor of four books and is the co-inventer of a U.S. patent. He has presented up to 11 keynote speeches in international conferences. His main research interests include the design of new topologies of ac machines and the implementation of advanced and efficient control strategies in drives and generators, applied to automotive as well as to renewable energy systems.

Prof. Masmoudi has been the Chair of the Program and Publication Committees of the International Conference on Ecological Vehicles and Renewable Energie (EVER), annually-organized in Monaco, since 2007. He is the Chair of the Founding, the Technical Program, and the Publication Committees of the International Conference on Sustainable Mobility Applications, Renewables, and Technology (SMART) that has been organized in the Australian College of Kuwait, in November 2015, and will be organized remotely, in November 2022.